Contents

List of Figures

Chapter 3

Observations and data reduction

The basis for this thesis are radio and X-ray observations of NGC 1052. The observations have been performed by three different instruments; the VLBA (Very Long Baseline Array), a telescope array of 10 antennas in the USA; MERLIN (Multi–Element Radio–Linked Interferometer Network), a connected array of telescopes in Great Britain; and the X-Ray satellite CHANDRA. The VLBA observations were planned and scheduled in 1998 by Dr. A. P. Lobanov, who provided the obtained data for the purpose of this diploma thesis. The MERLIN and CHANDRA data were obtained from public archives in the Internet. Since this thesis focuses mainly on the VLBA data, only these observations and the underlying principle will be discussed here. MERLIN and CHANDRA will be presented in Appendix B as well as an outline of the corresponding data reduction.

I will start with a brief introduction of Very Long Baseline Interferometry (VLBI), the observing technique of the VLBA. The VLBA data reduction will be discussed in Section 3.3 . Both sections will be kept brief, since VLBI and in general radio interferometry is discussed in more detail in many textbooks as e.g., Thompson et al. (1986).

3.1 Fundamentals of radio aperture synthesis

Figure 3.1 shows the geometry of a simple radio interferometer consisting of two antennas, pointed at a distant radio source. If the source is far enough (in the so called far-field-pattern), the incoming rays to the different interferometer elements can be assumed to be parallel. Each of the two antennas registers a signal that produces voltages V_1 and V_2 in the telescope backend. These voltages are eventually correlated, i.e., a circuitry performs a multiplication and averaging of the (converted) voltages[1]. If the source is, for simplicity, a monochromatic emitter, then V_1 and V_2 both are sinusoidal functions. Figure 3.1 shows that the cosmic signal reaches the first antenna at a time $\tau_{\mathrm{g}} = (D/c)\cos\theta$ before it arrives at the second one, where D is the baseline of the two telescopes and c is the velocity of light. This is called the geometrical delay and the correlator output is proportional to

$$F = \sin(2\pi\nu t)\sin(2\pi\nu[t-\tau_{\mathrm{g}}]) \quad . \tag{3.1}$$

[1]In contrast to the simple adding interferometer, which basically receives the quantity $(V_1 + V_2)^2$, the correlator interferometer is proportional only to the correlated component of the two signals. The uncorrelated components cancel out during the time averaging process. This leads to a substantial reduction of noise in the output.

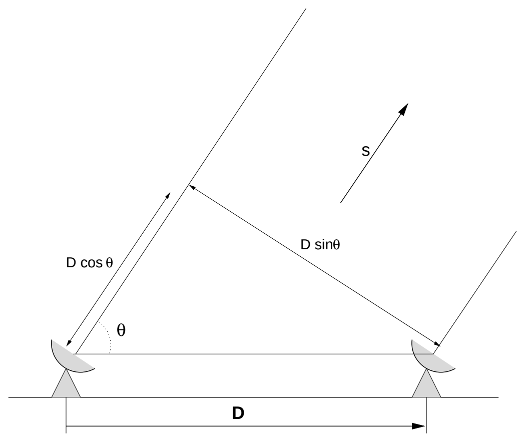

Figure 3.1: An elementary radio interferometer. Taken from Ros (1997).

Since the Earth rotates, the projected baseline $D\sin\theta$ varies with time and so does the geometrical delay. The terms independent of $\tau_{\rm g}$ can be filtered out, leaving for the correlator output (after some trigonometrical transformations)

$$F = \cos\left(2\pi\nu\tau_{\rm g}\cos\theta\right) \quad . \tag{3.2}$$

Therefore, the correlator output is proportional to a quasi-sinusoidal fringe pattern[2], due to the rotation of the Earth. If the cosmic source is not a point source, but has extended structure, the interferometer receives the signal not only from the direction $\vec{s}$, where it is pointed at, but from a whole area around a nominal position $\vec{s}_0$. From the position $\vec{s}=\vec{s}_0+\vec{\sigma}$, an element of solid angle $d\Omega$ of the source then contributes the power $1/2\Delta\nu B(\vec{\sigma})A(\vec{\sigma})d\Omega$ at each of the two antennas. $\Delta\nu$ is the observing bandwidth, $B(\vec{\sigma})$ is the brightness at position $\vec{\sigma}$, $A(\vec{\sigma})$ is the reception pattern of the antenna, and the factor $1/2$ represents the capability of a telescope to receive only one direction of circular polarization. Correlating the two antenna output powers and applying the fringe term of Equation (3.2), the interferometer output becomes

$$\begin{aligned} r(\vec{D}_\lambda,\vec{S}_0) &= \Delta\nu\int_{4\pi}A(\vec{\sigma})B(\vec{\sigma})\cos(2\pi\vec{D}_\lambda\cdot\vec{s})d\Omega \\ &= \Delta\nu\cos(2\pi\vec{D}_\lambda\cdot\vec{s}_0)\int_{4\pi}A(\vec{\sigma})B(\vec{\sigma})\cos(2\pi\vec{D}_\lambda\cdot\vec{\sigma})d\Omega \\ &- \Delta\nu\sin(2\pi\vec{D}_\lambda\cdot\vec{s}_0)\int_{4\pi}A(\vec{\sigma})B(\vec{\sigma})\cos(2\pi\vec{D}_\lambda\cdot\vec{\sigma})d\Omega \end{aligned} \tag{3.3}$$

with $\nu\tau_{\rm g}=\vec{D}_\lambda\cdot\vec{s}$, where $\vec{D}_\lambda$ is the vector of the baseline in units of the observing wavelength. Introducing a complex quantity

$$V = |V|\mathrm{e}^{i\Phi_V} = \int_{4\pi}A_N(\vec{\sigma})B(\vec{\sigma})\mathrm{e}^{-i2\pi\vec{D}_\lambda\cdot\vec{\sigma}}d\Omega \tag{3.4}$$

[2]In reality a cosmic signal is never just composed out of one single frequency. The interference between different frequency components causes a modulation of the fringe function, which also depends on θ. This so called fringe-washing function has the shape of a sinc–function envelope, in the special case of a uniform power spectral density.

with a normalized reception pattern $A_N(\vec{\sigma}) = A(\vec{\sigma})/A_0$, where A_0 is the antenna collecting area in direction $\vec{s}_0$, the correlator output is

$$r(\vec{D}_\lambda, \vec{S}_0) = A_0 \Delta\nu |V| \cos(2\pi \vec{D}_\lambda \cdot \vec{s}_0 - \Phi_V) \quad . \tag{3.5}$$

V is called the complex visibility. The correlator output can be expressed in terms of a fringe pattern with the modulus and phase of V. The phase is measured relative to the phase of a hypothetical fringe pattern, received from a point source at the position $\vec{s}_0$. Both, modulus and phase of V are observables, and Equation (3.4) shows that the visibility is the Fourier transform of the brightness distribution $B(\vec{\sigma})$. In order to reconstruct B, the visibility V has to be measured with different baselines $\vec{D}_\lambda$. Usually this is expressed in terms of a two-dimensional plane with coordinates $u = \vec{D}_\lambda^{E/W} \cos\theta$ and $v = \vec{D}_\lambda^{N/S} \cos\theta$, which are basically the projected baselines in east–west and in north–south direction and are called spatial frequencies. This (u, v)–plane has to be sampled frequently enough in order to be able to perform a discrete Fourier transform[3] of the measured visibility function $V(u, v)$ and thus retrieve the brightness distribution B of the source with an angular resolution determined by the highest spatial frequency of the interferometer.

3.2 Observations of NGC 1052 with the VLBA

The VLBA is a dedicated VLBI array of ten antennas across the US. It was built to overcome some of the problems that early VLBI experiments suffered from, namely limited observing time, not optimized locations and difficulties in data calibration due to inhomogeneity of the different antennas. The longest baseline of the VLBA (about 8600 km) is between the western most antenna at Mauna Kea on Hawaii and the eastern most one at St. Croix on the Virgin Islands. The location of the 10 (nearly identical) antennas, each of 25 m in diameter, is shown in Figure 3.2. VLBA observations are possible between 21 cm and 0.35 mm wavelengths. The details of the VLBA design and technical properties are reviewed by Napier (1994).

NGC 1052 was observed on December 28th 1998 with all 10 antennas of the VLBA at four frequencies (5, 8.4, 22.2 and 43.2 GHz) in dual polarization mode. The data were recorded with a bit rate of 128 Mbps at 2-bit sampling providing a bandwidth of 16 MHz per polarization hand (divided in 2 blocks of 16 0.5 MHz channels each). The total integration time on NGC 1052 was about one hour at 5, 8.4, and 22.2 GHz each, and about six hours at 43.2 GHz, to compensate the lower array-sensitivity and the lower source flux density at this frequency. 3C 345 and 0237+28 were used as calibrators during the observation. A standard correlation was done at the Array Operations Center of the VLBA in Socorro NM, US, with an averaging time of two seconds and the data were distributed as a DAT tape. The performance of the array was very good during the observations. The Owens Valley antenna did not record data at 8.4 and 22.2 GHz. The high frequency data at 22.2 and 43.2 GHz suffered from some snow in the Brewster dish and rain at St. Croix.

[3]According to the sampling theorem a discrete Fourier transformation, as an approximation to a continuous Fourier transformation of an analytically given function, can be done, if the sampling frequency is at least twice the frequency of the highest spatial frequency.

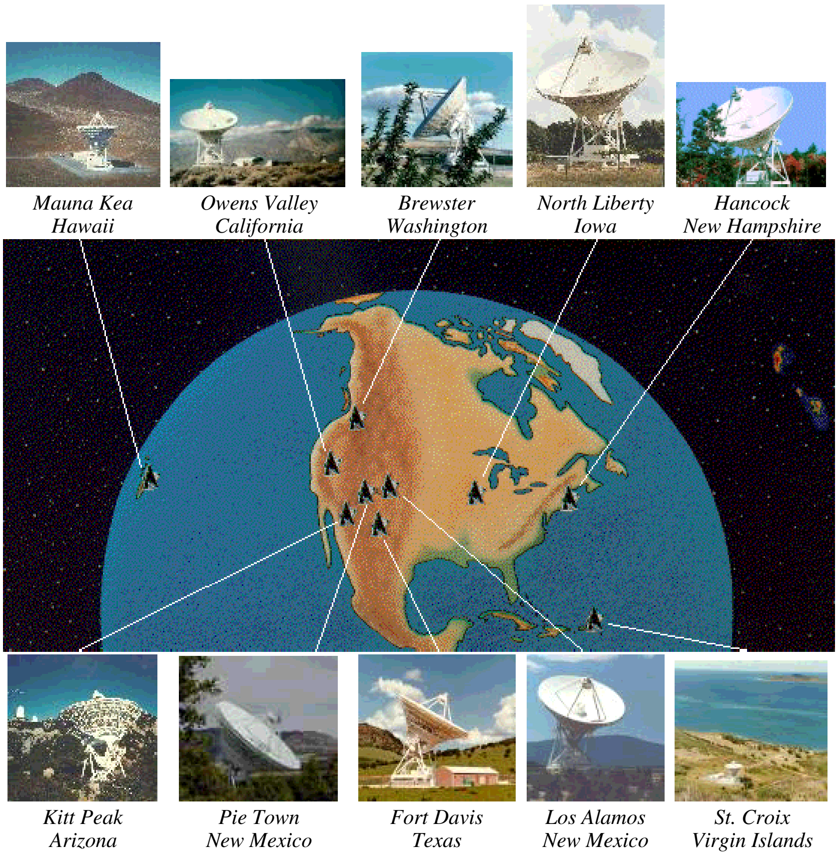

Figure 3.2: The antennas of the VLBA. Taken from the NRAO website (`http://www.nrao.edu`).

3.3 VLBI data reduction

VLBI data analysis requires a complex post-processing before the brightness distribution of the target source and its polarimetric properties can be obtained. This section describes the different steps of data reduction, performed to derive the astronomical information, discussed in chapter 4 . The first part of the data reduction was done in $\mathcal{AIPS}$ (Astronomical Image Processing System; Fomalont 1981). After this *a–priori* calibration the visibility-data were exported and further processed in DIFMAP (Pearson et al. 1994). In this part, the brightness distribution of NGC 1052 was derived. From the information about the source structure in total intensity, the polarimetric properties of the source were obtained using $\mathcal{AIPS}$ routines. These three steps are described briefly as follows.

Pre–calibration data processing: Using the task FITLD the data were read from the VLBA correlator distribution tape into $\mathcal{AIPS}$. During this procedure, the visibilities with low weight in the correlation process (due to a poor signal to noise ratio (SNR) of the detected fringes) were flagged. The visibilities were sorted according to their baseline and time stamp order using the task MSORT. The task INDXR produces an index table which can be read in from other tasks in order to get a faster access to the visibilities of a special time and/or baseline.

As a reference antenna, with respect to whose fringes the phases are taken, LA (Los

Álamos) was chosen for all four frequencies since it had good data for the whole experiment and had also the benefit that it is located in the center of the array, providing both short and long baselines.

After this, the visibilities have to be examined carefully to get a "feeling" for the data quality and find bad data points to be flagged due, for example, to recording or bandpass problems at a single antenna. The task POSSM, e.g., allows one to plot the measured visibilities against frequency, divided by 16 channels in two frequency bands (IFs). Degraded data at the upper edge of both IFs, namely in channel 15 and 16, required the flagging of the corresponding data. The tasks VPLOT, UVPLT and SNPLT offered additional possibilities of data examination that will not be described here in detail.

The calibration of the data in $\mathcal{AIPS}$, described in the next paragraphs, is based on the following "philosophy": the data themselves are not modified during the calibration process. In each incremental step of data calibration, conversion factors are determined and stored in a separate file, called a solution table (SN). After the next calibration step a second SN table is produced and stored. The task CLCAL is used to produce a calibration table (CL) with the combined conversion factors, calculated from the two separate SN tables. In each additional calibration step a new SN table is produced and CLCAL calculates a new CL table from the previous one and the new SN table. Each SN table represents an individual calibration step and each CL table contains the combination of all the calibration steps performed so far. If it becomes necessary during the data calibration to flag single data points or regions of data, the corresponding information is stored in flag tables (FG). Only at the very end of the calibration process in $\mathcal{AIPS}$ the latest CL table and the most complete FG table are applied to the data. The benefit of this principle is that it is possible to redo a special calibration step without the need to throw away the solutions corresponding to the following calibration steps. So it is easy to correct errors that might have happened and are detected in a later stage of the data reduction.

A-priori **amplitude calibration:** In the first part of the data calibration the amplitudes of the visibility data points are corrected for instrumental effects. The visibility amplitudes can be expressed in terms of a correlation coefficient ρ, which is equal to one if the signals at the two telescopes are totally correlated, i.e., if they are identical, and which is equal to zero if the signals are totally uncorrelated. The case $\rho = 1$ corresponds to an idealized observation of a point source. A fully resolved, extended structure corresponds to ρ=0. The measured visibility V_{m} then can be expressed as

$$V_{\mathrm{m}} = \rho\, b \sqrt{\frac{T_{\mathrm{sys},i}}{T_{\mathrm{sys},j}} K_i K_j} \quad , \tag{3.6}$$

where b describes losses in the digitalization process of the signal. For dual-polarization observation data, the b factors can be determined from the amplitude offsets between the RR (the right hand polarization signal of the first antenna correlated with the right hand polarization signal of the second antenna) and LL (correlation of the left hand signals) visibilities. This is done with the task ACCOR, which produces a solution table (SN) with the necessary correcting factors. $T_{\mathrm{sys},i/j}$ are the system temperatures of the two telescopes and $K_{i/j}$ the corresponding sensitivities. Since the system temperature, the antenna sensitivities and the digitalization losses can be derived from calibration measurements of known sources, the correlation coefficient ρ and the "true" visibilities can be reconstructed. To do this in practice a so called radiometry file has to be produced, which contains the necessary antenna information. Two files containing the system temperatures and the gain curves (the elevation-dependent antenna sensitivities) were retrieved from the VLBA-observations archive[4]. The gain curves are contained in the file `vlba_gains.key`, which has to be edited, according to the epoch of the observation. The system temperatures are concatenated to the same file and from this radiometry file the information is read into a gain-curve table (GC) and a system temperature table (TY) in $\mathcal{AIPS}$ using the task ANTAB. The task APCAL produces from those a solution table (SN). The task CLCAL applies the correcting factors of the first SN table to the first CL table and produces a second calibration table (CL). A second run of CLCAL produces a third CL table containing the combined correction factors of both SN tables with the necessary corrections to get *a–priori* amplitude calibrated visibilities.

If at any step of the data reduction the examination of the data reveals bad regions of data, for example time ranges, channels or single points, the task UVFLG can be used to flag these data. The inspection of the system temperatures (task SNPLT) showed for example that one antenna had collected about one hour of data with unusually high system temperatures. This was due to a very low elevation of the target source. This region of data has been flagged for the corresponding frequency and the flagging information was written into a flag table (FG).

***A–priori* phase calibration:** Since the right circular polarization (RCP) and left circular polarization (LCP) feeds of an antenna rotate in position angle with respect to a source during an experiment (Earth rotation) this contribution to the phases had to be removed first (parallactic angle correction). For this purpose the task CLCOR was applied to a copy of the most recent CL table, since CLCOR directly affects the CL table entries.

The measured visibility phases are affected by instrumental offsets and slopes between and within the different frequency channel bands (IFs). These phase offsets and gradients are caused by the passage of the signal through the electronics of the VLBA baseband converters and can be determined from so called phase–cal signals that had been injected into the data stream during the data recording process. Appropriate corrections have to be applied to the data, to permit to average the visibilities over frequency and time. The phase-cal information can be read into $\mathcal{AIPS}$ from an external file using the task PCLOD, which produces a first phase-cal table (PC). The task PCCOR was used to calculate a SN table from the entries of the PC table for the four frequencies separately, that can be used to correct for the instrumental single-band phase and delay offsets. For this purpose a “good” scan was chosen, that contained a data point on a calibrator for every antenna and a corresponding entry in the PC table. This should solve for any 2π ambiguities. The phase rates were set to zero with task SNCOR and the resulting SN table was applied to the most recent CL table with CLCAL. After this calibration step the visibility phase as a function of frequency is smooth and shows no sharp jumps anymore.

Fringe fitting: After correcting the visibility phases for instrumental effects in the *a–priori* phase calibration, small residual phase errors remain in the data, due to propagation effects in the Earth/s atmosphere and inaccurate modeling of the geometry of the interferometer. This results in a phase gradient between the wavebands, measured as the

[4] `ftp://ftp.aspen.nrao.edu`

multi-band delay, in contrast to the single-band delay, that has been calibrated in the *a–priori* calibration. There are however, residual single-band delays that could not be removed in the *a–priori* phase calibration. The residual errors are larger at higher frequencies. Those can be inspected using the tasks POSSM (showing the visibility averaged in time as a function of frequency) and VPLOT (averaged in frequency as a function of time). Both rates were removed with the task FRING to make the data ready for averaging in time and frequency. The last CL and FG tables were specified to perform this task. LA (Los Álamos) was again chosen as the reference antenna and the sequence of the fringe fitting on the different baselines was specified, so that the fitting was done first on short baselines with high flux density and good SNR. This prevents the loss of data from a whole antenna if no solution is found at first instance. The two polarization hands were treated separately for each frequency. The time and frequency intervals that should be searched for fringes had to be specified as a compromise between a bad signal to noise ratio (with small windows) and the loss of coherence (with too big windows). The derived solutions can be checked for consistency using the task SNPLT and edited when necessary with the tasks SNSMO or SNEDT. Figure 3.3 shows the visibilities of a scan on NGC 1052 for a single baseline (Kitt Peak – North Liberty) as a function of frequency after the fringe fitting and shows that the data after this calibration are now ready for averaging. The amplitudes are smooth and the phases show no offsets or slopes.

The last CL table with the complete calibration information had finally to be applied

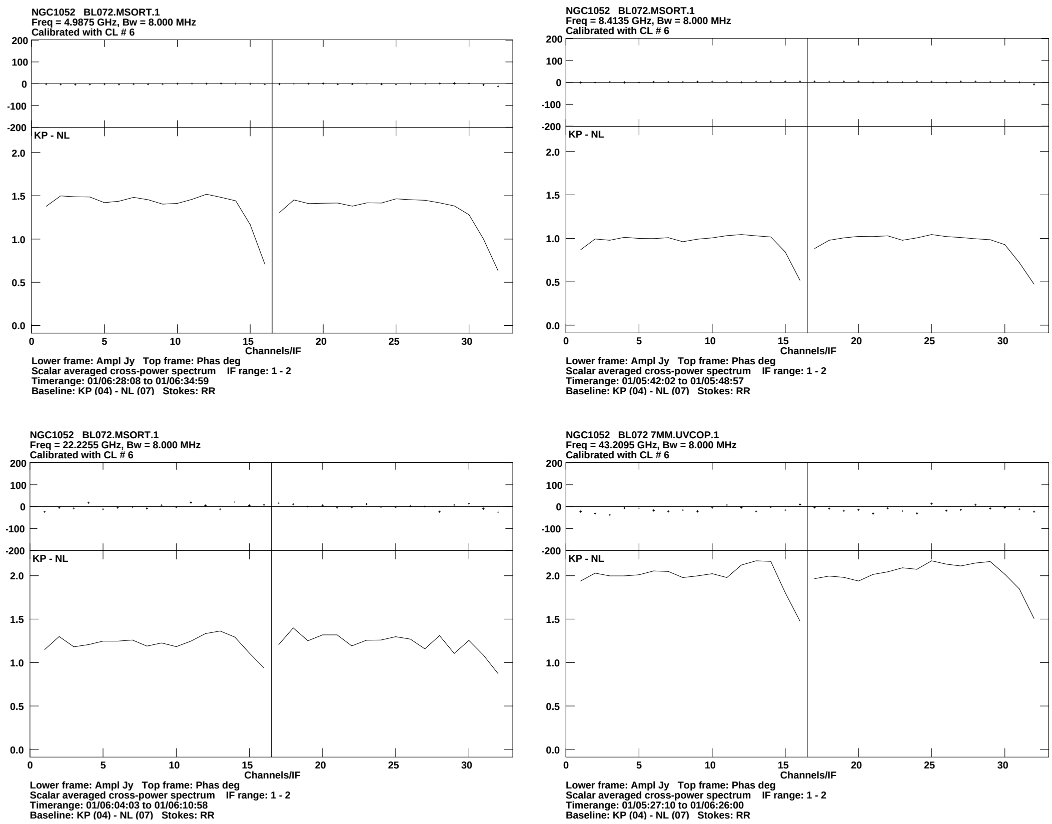

Figure 3.3: A POSSM plot of one scan on the baseline Kitt Peak – North Liberty for each of the four frequencies showing fringe-fitted data as a function of frequency.

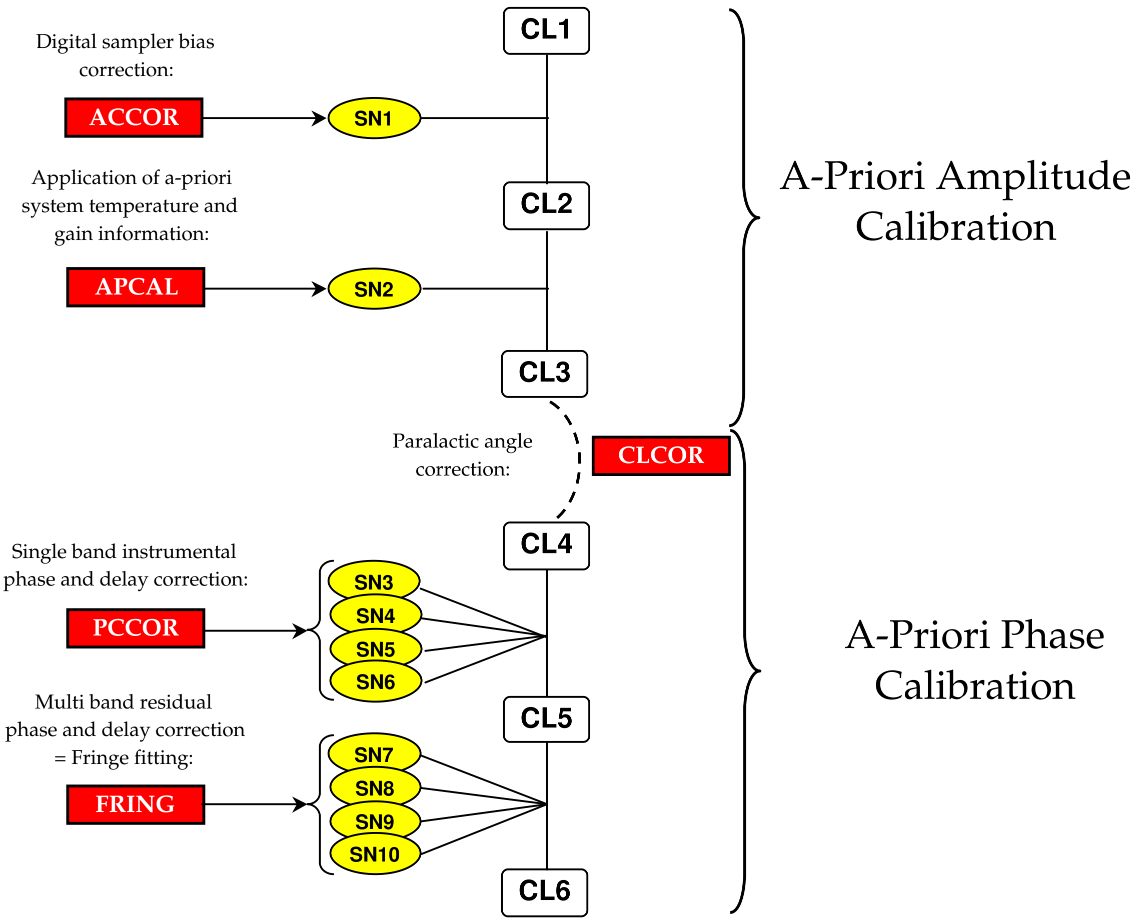

Figure 3.4: The basic path of data *a–priori* calibration in $\mathcal{AIPS}$.

to the data using the task SPLIT. In this step a calibrated data set for each source at each frequency is produced and these data sets are exported from $\mathcal{AIPS}$. Figure 3.4 summarizes the various calibration steps performed within $\mathcal{AIPS}$ in a flux diagram.

Data self–calibration and mapping the total intensity distribution: The data output from $\mathcal{AIPS}$ is in the FITS format (Wells et al. 1981) and can be read in by the program DIFMAP (Pearson et al. 1994), an interactively editing and mapping program. DIFMAP provides a variety of possibilities to plot and edit the (u, v)–data, yielding a more user-friendly access to the data than $\mathcal{AIPS}$.

At this point the data are organized in one-source files for each frequency and in the case of full polarization data in different data streams for RCP and LCP. To map the total intensity the data stream 'I' has to be chosen. The commands UVPLOT and TPLOT provide information about the (u, v)–coverage and the time coverage of the observation. Examples for both are given in Figure 3.5 and 3.6 for the case of the 43 GHz data of NGC 1052. The structure of the measured visibilities as a function of time and (u, v)–distance can be examined with the commands RADPLOT, VPLOT and PROJPLOT.

The (u, v)–data have to be Fourier-transformed to derive the brightness distribution of NGC 1052 at the four frequencies. Since the two-dimensional visibility function is

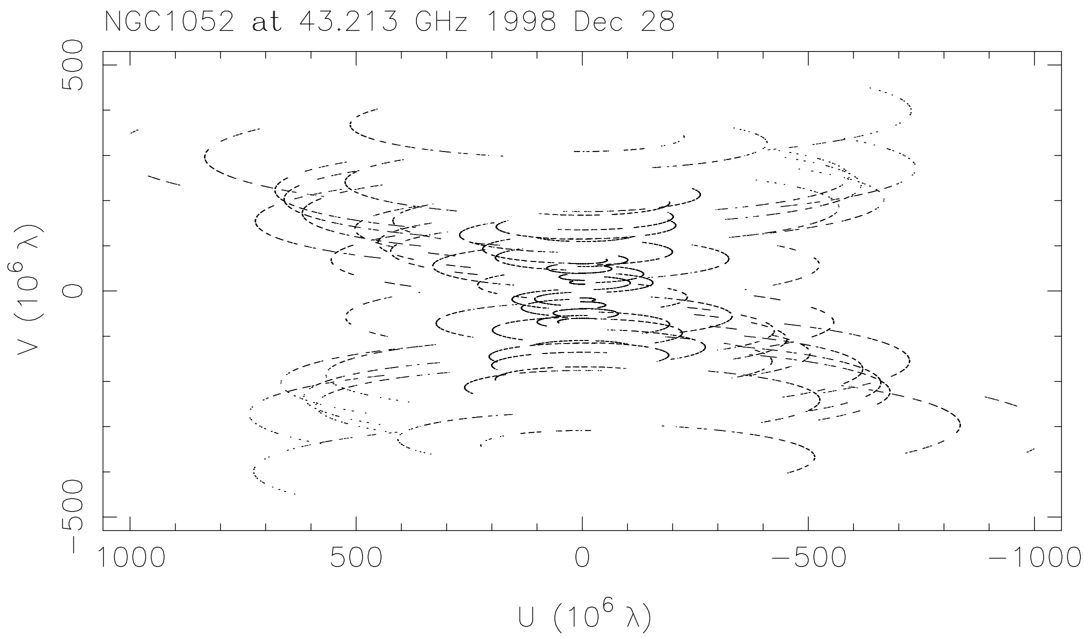

Figure 3.5: A (u, v)–plot, showing the location of baselines in the (u, v)–plane during the 43 GHz observation of NGC 1052

measured only at 45 points in the (u, v)–domain[5] during one integration bin, the discrete Fourier transform algorithm has to be used, to derive an approximation to the true Fourier transform of this function:

$$B'(x, y) = \sum_{j=1}^{M} V(u_j, v_j) \exp^{2\pi i(u_j x + v_j y)} \tag{3.7}$$

with

$$V(u_j, v_j) = V(u, v) \cdot w_j; \qquad w_j = \begin{cases} 1 & : \quad u = u_j, v = v_j \\ 0 & : \quad u \neq u_j, v \neq v_j \end{cases}$$

The result of this procedure is the “dirty map”, which is the convolution of the true brightness distribution $B(x, y)$ with the reception pattern of the array, the “dirty beam”. The “dirty beam” is composed of a central peak with the full width at half maximum (FWHM) of $(u_{max} \cdot v_{max})^{-1/2}$ and a number of weaker, local maxima, which are due to the imperfect sampling of the (u, v)–plane. The better the sampling is, the less prominent are these local maxima. Different algorithms have been developed to deconvolve the “dirty map”, the CLEAN algorithm (Högbom 1983) being the most extended. In each step of this iterative algorithm a fraction (loop gain) of the “dirty beam”, a CLEAN component, is subtracted from the “dirty map” at the position of its maximum. The position and flux of the CLEAN component is stored temporarily as well as the modified “dirty map”, without the contribution of the CLEAN component, now called the residual map. In this residual map the new maximum is searched and another cycle of “cleaning” is applied. This algorithm should make the residual map smooth and featureless. In a final step, the temporary map that contains the CLEAN components has to be convolved

[5]A telescope array of N antennas provides $N(N-1)/2$ baselines. For the VLBA and its 10 antennas this results in 45 baselines.

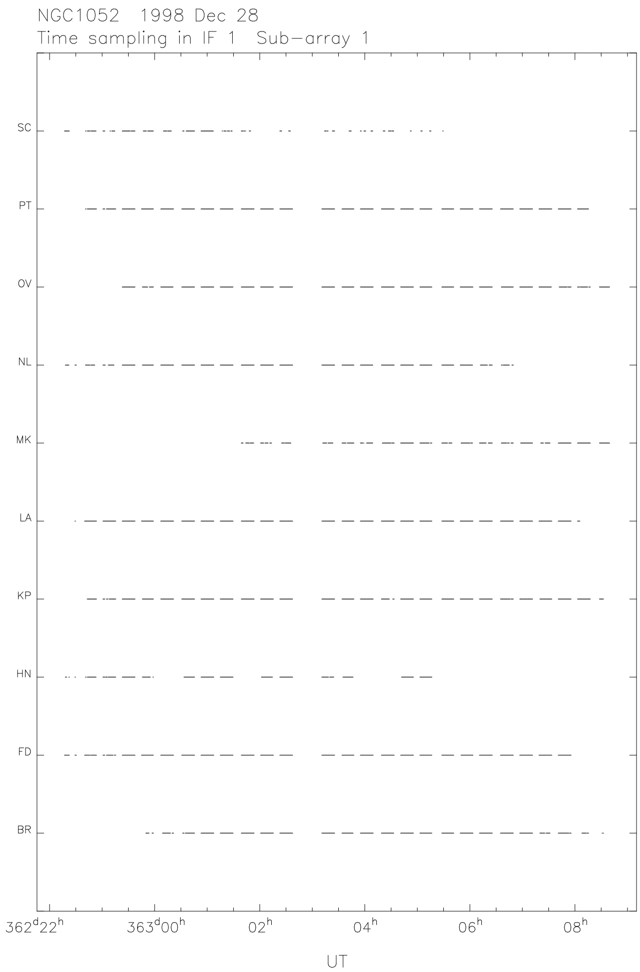

Figure 3.6: Time coverage of the NGC 1052 observation at 43 GHz.

with an idealized interferometer beam (equivalent to the diffraction pattern), which is a two-dimensional Gaussian function with the FWHM of the "dirty beam". The residual map is added to this "CLEAN map", resulting to a final map, which represents the true brightness distribution as approximated from the measurements. The choice of a loop gain smaller than one in each cycle ensures that no artificial effects arise in the "clean map".

The quality of the final map can be enhanced, using the self consistency of the data and the derived model, by self–calibration. Even after the *a–priori* calibration of the data in $\mathcal{AIPS}$, both the amplitudes and the phases of the visibilities are affected by errors. The measured phases can be written as

$$\Theta'_{i,j} = \Theta_{i,j} + \Phi_i - \Phi_j + \epsilon_{i,j} \quad , \tag{3.8}$$

with $\Theta_{i,j}$ the true phase, $\Phi_{i/j}$ an error contribution arising at station i and j, respectively, and a noise term ϵ. The influence of the station-dependent terms cancel out if the sum of three different stations are added up:

$$\Theta'_{i,j} + \Theta'_{i,k} + \Theta'_{j,k} = \Theta_{i,j} + \Theta_{i,k} + \Theta_{j,k} + \epsilon_{i,j} + \epsilon_{i,k} + \epsilon_{j,k} \tag{3.9}$$

This closure-phase relationship is used in the phase self calibration that can be applied between the subsequent CLEAN steps. The visibility phases are varied in order to best fit the derived model, keeping the closure phases constant.

The CLEAN algorithm is implemented in DIFMAP and can be applied with the command CLEAN N, L, where N is the number of CLEAN iterations to perform, each with a loop gain L. After a CLEAN cycle, phase self–calibration is applied with the command SELFCAL. When the iteration has converged, i.e., when the "cleaned" flux no longer increases and/or the residual map has become smooth and featureless, the derived model can be used to self–calibrate the visibility amplitudes. After this, the mapping process starts from the beginning, but now using the better calibrated data.

The (u, v)–data of NGC 1052 at the four frequencies have been mapped according to this strategy. After reading in the data, they were averaged into 30 second bins to accelerate the mapping process. The data were examined using the commands VPLOT, which shows the visibilities as a function of time for each baseline, and CPPLOT, which displays the closure phases for the various triangles of telescopes. Any obviously bad data points were flagged. Starting from a point source model the "dirty map" at each frequency was "cleaned" and the data were phase self–calibrated. In this first cycle each data point was given the same weight (natural weighting). This overemphasizes the short (u, v)–spacings, which are more frequently sampled in the (u, v)–plane and prevents one from loosing extended structures.

After obtaining a first good model, the data were amplitude self–calibrated for a first time with the command GSCALE. In this procedure time-independent gain factors for each antenna are determined, which increase the consistency between the data and the model. These factors are given in the output of GSCALE and should be small. For 5 and 8.4 GHz the performance was excellent, with correction factors not bigger than 2% with a mean of 0.9% and 0.6%, respectively. At 22 GHz the biggest correction of 4% was applied to the antenna at St. Croix and the mean correction was about 2%. At 43 GHz the antenna at Mauna Kea needed a rather big correction of 29% but the other antennas also had a remarkably good *a–priori* calibration at this very high frequency with correction-factors below 5%. Having this amplitude self–calibrated data set, the "cleaning" and phase self–calibration process was restarted from a point-source model. At the end of this second cycle a second amplitude self–calibration was performed with a time scale of 180 minutes. The time dependent correction factors were examined with the command CORPLOT.

In the following iterations the time scale was decreased further in 8 steps, down to a time scale of 1 minute. From the second cycle on, uniform weighting was chosen, which gives the weights in the (u, v)–plane according to the local density of data points. Uniform weighting gives the best angular resolution but reduces the sensitivity of the array. In the last cycle the amplitudes were allowed to vary freely and a fully amplitude and phase self–calibrated dataset was saved. From this the final map for each frequency was produced.

Figure 3.7 shows the visibilities of the 43 GHz observation of NGC 1052 as a function of time for the baseline Fort Davies to Pie Town at the beginning and at the end of the self–calibration process. In Figure 3.8 the final 5 GHz data set is plotted as a function of radial (u, v)–distance projected on two one dimensional slices along a position angle (P.A.) of 69° (parallel to the VLBI jet) and 159° (perpendicular to the axis of the VLBI jet), respectively. Along P.A.=69° the visibility shows fringes indicating at least two strong and interfering components. Perpendicularly to this, no obvious structure can be seen from the (u, v)–data. The good agreement between the model and the data also allowed to derive a model visibility distribution in the (u, v)–plane as the Fourier transform of the

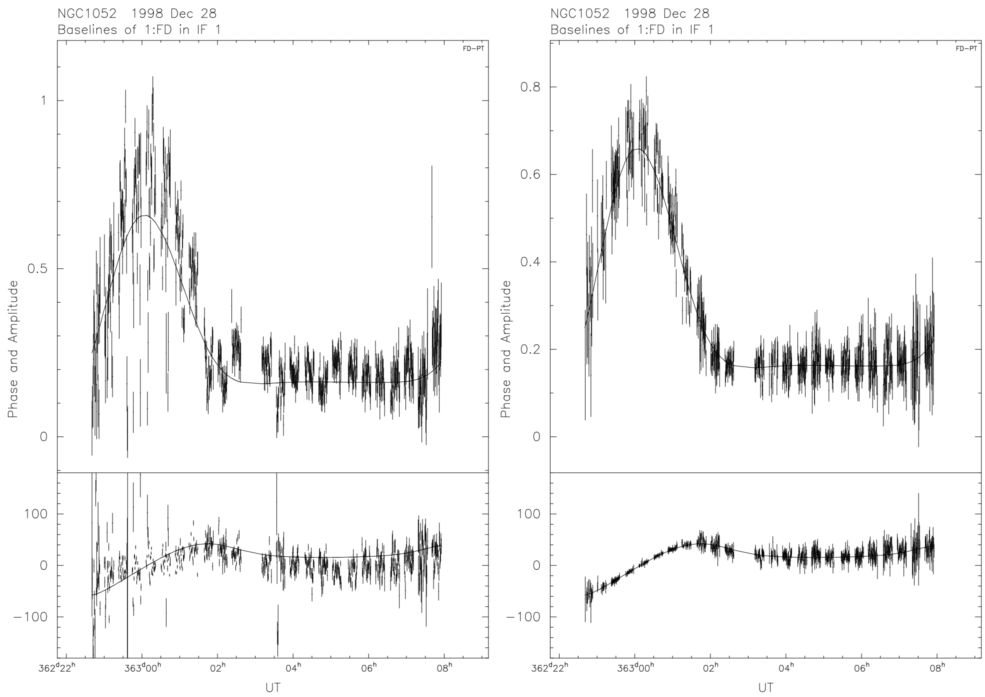

Figure 3.7: 43 GHz Visibility amplitude (top) and phase (bottom) versus time on the baseline FD–PT. Left: *A–priori* calibrated data; Right: Edited and fully calibrated data. The data are shown as points with error bars, and the final model is plotted in both cases as a continuous line.

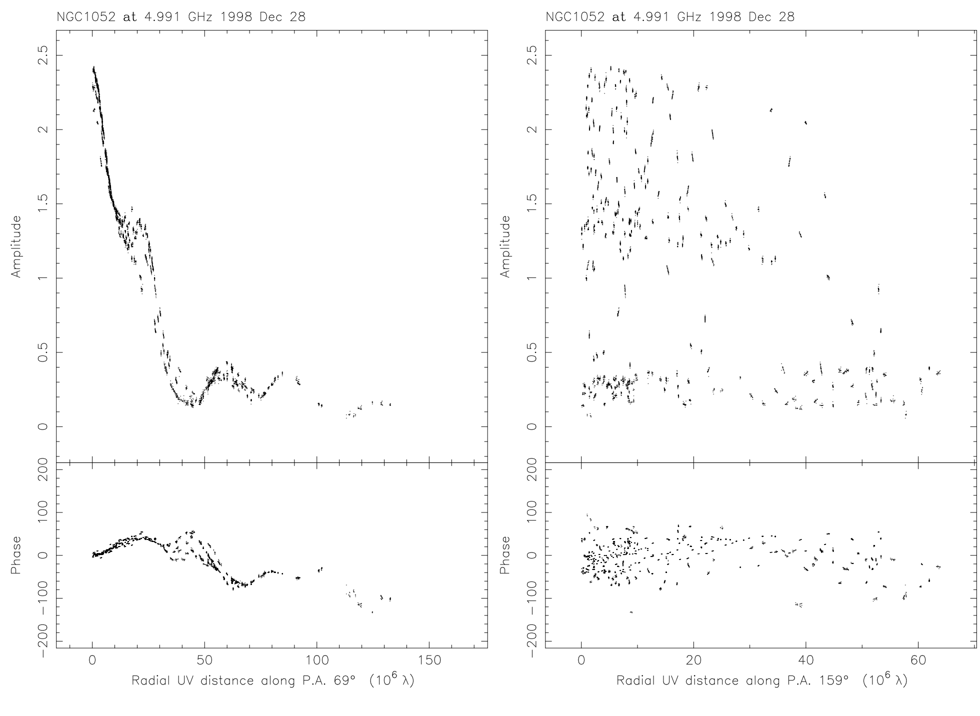

Figure 3.8: The visibility distribution projected on two perpendicular planes in the (u, v)–plane. The local maxima, visible in the left panel (P.A.=69°), correspond to the side-lobes of the visibility amplitude in the (u, v)–plane, in Figure 3.9.

model brightness distribution. Figure 3.9 shows contour plots of the brightness distribution ((x, y) domain) and the visibility amplitude ((u, v)–domain). The (u, v)–plane sampling points ((u, v)–coverage) at which the visibility was measured are shown superimposed on the model visibility amplitudes. The amplitude of the visibility is dominated by a central maximum (note the uneven contour levels given in the figure caption). Along P.A.=69° several side-lobes are prominent, corresponding to the fringes in Figure 3.8.

Polarization calibration and mapping the polarization structure: In very long baseline polarimetric (VLBP) observations the antenna feeds record circular polarization in both hands, RCP and LCP. From the observations of NGC 1052 in December 1998 the cross correlations r_{mn}^{RR}, r_{mn}^{LL}, r_{mn}^{RL} and r_{mn}^{LR} for each antenna pair m, n were formed in the VLBA correlator from the measured right circular and left circular polarized (RCP and LCP) signals. These cross correlations have to be corrected for instrumental effects, described in this paragraph, in order to derive the true visibilities $\mathfrak{RR}, \mathfrak{LL}, \mathfrak{RL}$ and $\mathfrak{LR}$. Following the discussion of Leppänen et al. (1995), the four Stokes parameters I, Q, U and V, which specify the polarimetric properties of the source radiation, can be obtained as the Fourier transform (indicated by $\rightleftharpoons$) of these correlations

$$\begin{aligned} \mathfrak{RR} &\rightleftharpoons I + V \\ \mathfrak{LL} &\rightleftharpoons I - V \\ \mathfrak{RL} &\rightleftharpoons Q + iU = P \\ \mathfrak{LR} &\rightleftharpoons Q - iU = P^* \quad , \end{aligned} \tag{3.10}$$

where $P = p\mathrm{e}^{2i\chi}$, with p the polarized intensity and χ the electric vector position angle (EVPA). Unfortunately, real antenna feeds do not exclusively register one single polarization, some leaking of the opposite hand is always present. This effect of instrumental polarization can be expressed in a model of the interferometer response (Kemball et al. 1995:

$$\begin{aligned} r_{mn}^{RR} &= g_m^R g_n^{R*} \{ \mathrm{e}^{-i(\alpha_m-\alpha_n)} \cdot \mathfrak{RR} + D_m^R \mathrm{e}^{i(\alpha_m+\alpha_n)} \cdot \mathfrak{LR} \} \\ &\quad + D_n^{R*} \{ \mathrm{e}^{-i(\alpha_m+\alpha_n)} \cdot \mathfrak{RL} + D_m^R D_n^{R*} \mathrm{e}^{i(\alpha_m-\alpha_n)} \cdot \mathfrak{LL} \} \\ r_{mn}^{LL} &= g_m^L g_n^{L*} \{ \mathrm{e}^{i(\alpha_m-\alpha_n)} \cdot \mathfrak{LL} + D_m^L \mathrm{e}^{-i(\alpha_m+\alpha_n)} \cdot \mathfrak{RL} \} \\ &\quad + D_n^{L*} \{ \mathrm{e}^{i(\alpha_m+\alpha_n)} \cdot \mathfrak{LR} + D_m^L D_n^{L*} \mathrm{e}^{-i(\alpha_m-\alpha_n)} \cdot \mathfrak{RR} \} \\ r_{mn}^{RL} &= g_m^R g_n^{L*} \{ \mathrm{e}^{-i(\alpha_m+\alpha_n)} \cdot \mathfrak{RL} + D_m^R \mathrm{e}^{i(\alpha_m-\alpha_n)} \cdot \mathfrak{LL} \} \\ &\quad + D_n^{L*} \{ \mathrm{e}^{-i(\alpha_m-\alpha_n)} \cdot \mathfrak{RR} + D_m^R D_n^{L*} \mathrm{e}^{i(\alpha_m+\alpha_n)} \cdot \mathfrak{LR} \} \\ r_{mn}^{LR} &= g_m^L g_n^{R*} \{ \mathrm{e}^{i(\alpha_m+\alpha_n)} \cdot \mathfrak{LR} + D_m^L \mathrm{e}^{-i(\alpha_m-\alpha_n)} \cdot \mathfrak{RR} \} \\ &\quad + D_n^{R*} \{ \mathrm{e}^{i(\alpha_m-\alpha_n)} \cdot \mathfrak{LL} + D_m^L D_n^{R*} \mathrm{e}^{-i(\alpha_m+\alpha_n)} \cdot \mathfrak{RL} \} \end{aligned} \tag{3.11}$$

In these expressions, the subscripts m, n denote different antennas, the superscripts R, L denote different polarizations and the parallactic angles are denoted by α. The g-factors represent the complex antenna gains and the D–terms the ratios of the received unwanted polarization to the received nominal polarization in the complex voltage response (or leaking between the polarization hands). Note that the D–terms are the only quantities in these formulae, which are not known from the *a–priori* calibration of the data in $\mathcal{AIPS}$. Especially the parallactic angle correction that has been performed (page 36) simplifies the formulae since this correction corresponds to the substitution

$$g_m^R \mathrm{e}^{-i\alpha_m} \rightarrow g_m^R, \quad g_m^L \mathrm{e}^{i\alpha_m} \rightarrow g_m^L, \tag{3.12}$$

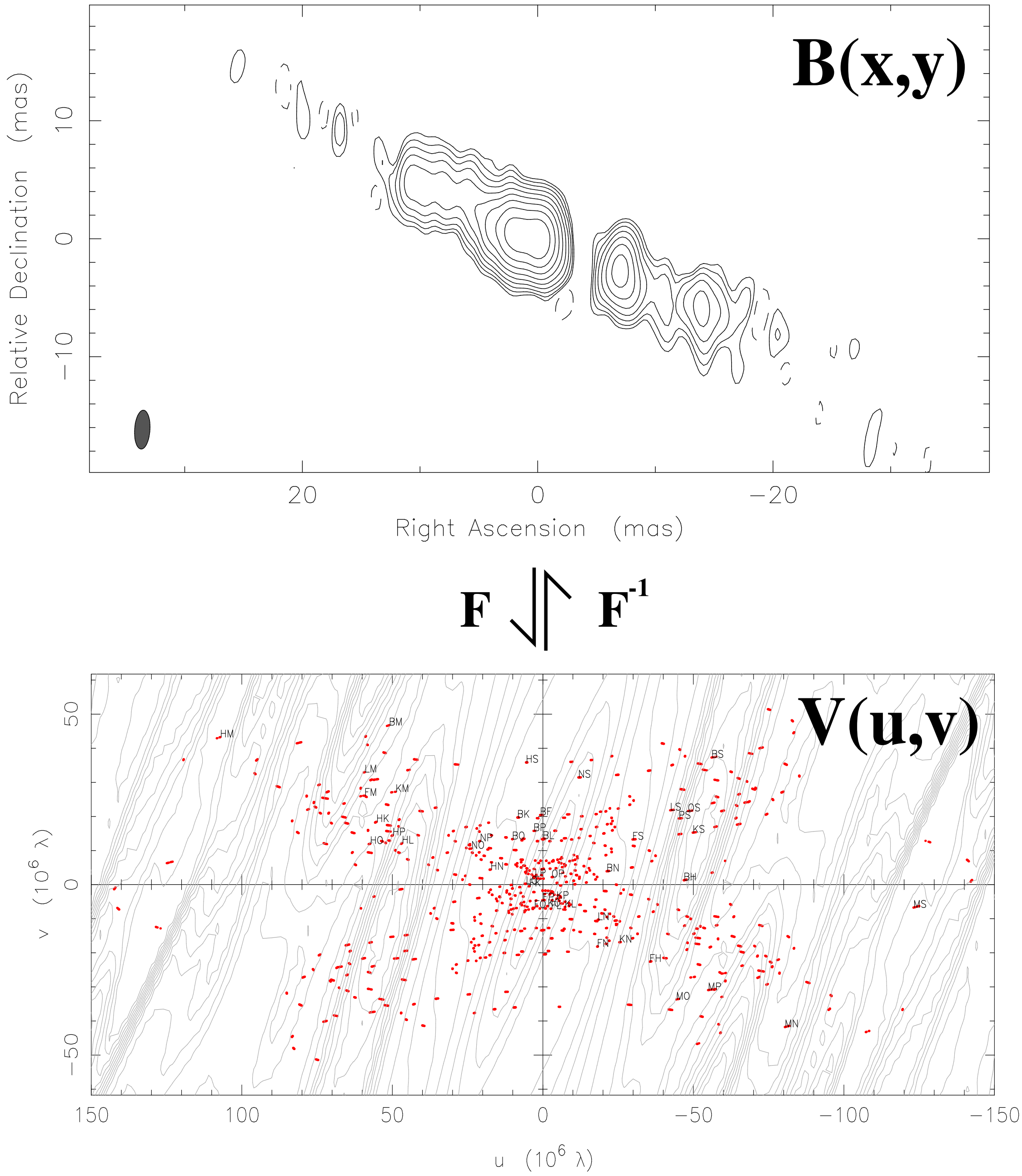

Figure 3.9: Top: Contour image of the brightness distribution ($B(x, y)$) of NGC 1052 at 5 GHz. Bottom: Contour plot of the (real part of the) Fourier transform of the brightness distribution, the visibility amplitude in the (u, v)–plane. The contours for 0.1, 0.125, 0.15, 0.175, 0.2, 0.225, 0.25, 0.275, 0.3, 0.35, 0.4, 0.6, 0.8, 1, 1.2, 1.4, 1.6, 1.8, 2, and 2.2 Jy are shown. Superimposed is the (u, v)–coverage during the experiment.

representing a rotation of the gain phases by the time dependent parallactic angle. A further simplification is achieved by neglecting second and third order terms in D, $\mathfrak{RL}$ and $\mathfrak{LR}$, since both the D–terms and the fractional polarization $\mathfrak{m} = P/I \propto \mathfrak{RL} \propto \mathfrak{LR}$ are small quantities. If additionally circular polarization is neglected ($\mathfrak{RR} = \mathfrak{LL} = \mathfrak{I} \rightleftharpoons I$) Equation (3.11) become

$$\begin{aligned} r_{mn}^{RR} &= g_m^R g_n^{R*} \cdot \mathfrak{I} \\ r_{mn}^{LL} &= g_m^L g_n^{L*} \cdot \mathfrak{I} \\ r_{mn}^{RL} &= g_m^R g_n^{L*} \{\mathfrak{RL} + (D_m^R \mathrm{e}^{2i\alpha_m} + D_n^{L*} \mathrm{e}^{2i\alpha_n}) \cdot \mathfrak{I}\} \\ r_{mn}^{LR} &= g_m^L g_n^{R*} \{\mathfrak{LR} + (D_m^L \mathrm{e}^{-2i\alpha_m} + D_n^{R*} \mathrm{e}^{-2i\alpha_n}) \cdot \mathfrak{I}\} \quad . \end{aligned} \tag{3.13}$$

Equations (3.13) represent a linearized model of the interferometer response in VLBP experiments. It is based on the assumption that the D–terms are small ($< 5\%$), which is usually true for observations made with the VLBA.

To the degree that these are valid assumptions, Equation (3.13) shows that the parallel-hand cross correlations (r_{mn}^{RR}, r_{mn}^{LL}) respond only to the total intensity I and the cross-hand correlations (r_{mn}^{RL}, r_{mn}^{LR}) are sensitive to linearly polarized intensity. Once the D–terms are known, the true visibilities $\mathfrak{RR}, \mathfrak{LL}, \mathfrak{RL}$ and $\mathfrak{LR}$ can be determined from Equation (3.13) and the degree of linear polarization $\mathfrak{m}$ and the EVPA χ from Equation (3.10):

$$\mathfrak{m} = \frac{\sqrt{Q^2 + U^2}}{I}, \quad \chi = \frac{1}{2} \cdot \arctan\left(\frac{U}{Q}\right) \tag{3.14}$$

The D–terms are complex quantities. Their modulus affect the degree of polarization and their phase determines the polarization plane. Equation (3.10) shows that the latter depends on the phase difference between the $\mathfrak{RL}$ and the $\mathfrak{LR}$ cross correlations. Since χ is determined by the difference of $\mathfrak{RL}$ and $\mathfrak{LR}$, an offset for both is usually allowed. Special care has to be taken therefore to calibrate the absolute EVPA of the radiation.

Leppänen et al. (1995) developed an algorithm to determine the instrumental polarization leakage factors and to separate the source and instrumental polarization, using the target source itself. This algorithm was applied to self–calibrate the polarization characteristics of the VLBA in the polarimetric observation of NGC 1052, since the polarization of the source was unknown and, especially at the high frequencies, no suitable calibrators were available. This calibration step, usually referred to as feed calibration, is described in this paragraph. The only assumption in this algorithm is the spatial coincidence of polarized emission (if any) with the total intensity emission. To account for this constraint, a model for the total intensity, available from imaging in DIFMAP (or IMAGR within $\mathcal{AIPS}$), is used. To allow structural differences between the polarized and the total intensity structure, this model is divided into sub–models, whose polarizations are characterized by complex coefficients $p_s = (Q_s + iU_s)/I_s$) for each sub-model with the total intensity I_s. Setting the gain terms to unity and substituting the true parallel hand visibilities ($\mathfrak{I} = \mathfrak{RR} = \mathfrak{LL}$) with the observed counterparts (r_{mn}^{LL} and r_{mn}^{RR}), which is allowed if the gain self–calibration in DIFMAP has worked properly, the cross hand terms in Equation (3.13) become

$$\begin{aligned} \tilde{r}_{mn}^{RL}(u,v) = &\quad \textstyle\sum_s p_s \mathfrak{I}_s(u,v) + D_m^R \mathrm{e}^{2i\alpha_m} r_{mn}^{LL}(u,v) + D_n^{L*} \mathrm{e}^{2i\alpha_n} r_{mn}^{RR}(u,v) \\ \tilde{r}_{mn}^{LR}(u,v) = &\quad \textstyle\sum_s p_s^* \mathfrak{I}_s(u,v) + D_m^L \mathrm{e}^{-2i\alpha_m} r_{mn}^{RR}(u,v) + D_n^{R*} \mathrm{e}^{-2i\alpha_n} r_{mn}^{LL}(u,v) \quad , \end{aligned} \tag{3.15}$$

with $\mathfrak{I}(u,v)$, the Fourier transform of I_s and the sum over all sub-models. A linear least–squares–fit to the measured cross polarized visibilities can determine the unknown factors

p_s and D_m. The details of this algorithm can be found in Leppänen et al. (1995) and shall not be discussed here. However, the way the model is divided does not affect the solution, as long as the model has enough degrees of freedom to fit the true distribution of polarized emission. This requires a good enough parallactic angle coverage and a not too complicated polarization structure of the source.

As already mentioned, a common offset in the RCP and LCP gains does not affect the quality of the fit, since it is only the difference between both which is taken into account. This leads to the need for an absolute calibration of the EVPA, which is actually affected by such a common offset. In principle the application of the phase-cal information with PCCOR during the *a–priori* calibration should have removed such ambiguities, but it is necessary to check this externally. The way the EVPA can be calibrated depends on the special observation characteristics, and in Section 4.5 it is described how this was actually obtained in the case of NGC 1052.

To perform the feed calibration using the described algorithm, the best CLEAN component model from the hybrid mapping process in DIFMAP, contained in a FITS file was read into $\mathcal{AIPS}$ for all four frequencies, using the task IMLOD. The model information is contained in a CLEAN component (CC) table of the image. Using this model the (u, v)–data were phase self–calibrated with the task CALIB. Bad data points were flagged, using the task CLIP, by setting appropriate clipping levels, known from the data examination within DIFMAP, for the four Stokes parameters. With the fully calibrated data a total intensity source model was obtained with the task IMAGR within $\mathcal{AIPS}$. The map-size, the cell-size, the number of iterations and the weighting of the data had to be specified, which were all known from the mapping procedure within DIFMAP. The resulting map was checked for consistency with the map produced by DIFMAP. From the $\mathcal{AIPS}$ image file the CC table was now subdivided into ten sub-CC tables with the task CCEDT. Specifying these ten sub-models, a linear approximation of the D–terms was performed with the task LPCAL, according to Equation (3.15), which writes the results into the antenna table (AN), to be examined with the task PRTAN. The determination of the D–terms yielded values below 5% (except SC at 22 and 43 GHz), and are shown in Table 3.1. With the knowledge of the D–terms the Stokes parameters Q, U and V can be mapped, with the same mapping parameters of IMAGR as for the Stokes I map. The phase calibration from CALIB guarantees the proper registration of the maps with different Stokes parameters. Maps of the polarized intensity were produced, combining the corresponding Q and U maps with the task COMB (to be plotted with the task PCNTR). In Section 4.5 the results are presented and discussed. The basic path of feed calibration in $\mathcal{AIPS}$ is plotted schematically in Figure 3.10.

Table 3.1: The D–terms of the VLBA antennas on Dec 28th 1998

Antenna	Feed pol. type	D_5^{a}	$D_{8.4}^{b}$	D_{22}^{c}	D_{43}^{d}
BR	RCP	$0.0041e^{i149.0}$	$0.0216e^{i148.1}$	$0.0268e^{i77.8}$	$0.0342e^{i286.3}$
(Brewster)	LCP	$0.0107e^{i50.9}$	$0.0086e^{i250.2}$	$0.0113e^{i146.4}$	$0.0376e^{i232.4}$
FD	RCP	$0.0086e^{i144.1}$	$0.0064e^{i64.9}$	$0.0043e^{i55.3}$	$0.0144e^{i281.7}$
(Fort Davis)	LCP	$0.0104e^{i39.3}$	$0.0138e^{i153.0}$	$0.0122e^{i46.1}$	$0.0163e^{i23.5}$
HN	RCP	$0.0115e^{i177.1}$	$0.0153e^{i79.3}$	$0.0290e^{i343.5}$	$0.0479e^{i232.9}$
(Hancock)	LCP	$0.0067e^{i45.6}$	$0.0152e^{i126.8}$	$0.0252e^{i146.9}$	$0.0355e^{i349.6}$
KP	RCP	$0.0137e^{i156.8}$	$0.0019e^{i176.1}$	$0.0250e^{i36.8}$	$0.0150e^{i248.8}$
(Kitt Peak)	LCP	$0.0136e^{i33.3}$	$0.0060e^{i123.3}$	$0.0123e^{i176.4}$	$0.0200e^{i225.2}$
LA	RCP	$0.0125e^{i149.2}$	$0.0046e^{i143.5}$	$0.0158e^{i310.7}$	$0.0225e^{i302.8}$
(Los Álamos)	LCP	$0.0115e^{i22.9}$	$0.0118e^{i178.4}$	$0.0083e^{i29.0}$	$0.0102e^{i217.8}$
MK	RCP	$0.0080e^{i188.7}$	$0.0017e^{i299.9}$	$0.0085e^{i235.6}$	$0.0493e^{i216.6}$
(Mauna Kea)	LCP	$0.0135e^{i348.8}$	$0.0114e^{i175.5}$	$0.0217e^{i42.9}$	$0.0124e^{i113.1}$
NL	RCP	$0.0196e^{i154.5}$	$0.0059e^{i58.8}$	$0.0346e^{i14.1}$	$0.0413e^{i331.8}$
(North Liberty)	LCP	$0.0134e^{i10.3}$	$0.0066e^{i107.3}$	$0.0289e^{i164.1}$	$0.0299e^{i193.5}$
OV	RCP	$0.0063e^{i155.9}$	–[e]	–[e]	$0.0224e^{i100.7}$
(Owens Valley)	LCP	$0.0068e^{i7.9}$	–[e]	–[e]	$0.0287e^{i344.7}$
PT	RCP	$0.0121e^{i163.1}$	$0.0098e^{i192.1}$	$0.0082e^{i158.4}$	$0.0239e^{i275.4}$
(Pie Town)	LCP	$0.0203e^{i17.8}$	$0.0086e^{i19.6}$	$0.0155e^{i192.7}$	$0.0350e^{i74.5}$
SC	RCP	$0.0071e^{i225.0}$	$0.0152e^{i168.8}$	$0.0609e^{i195.3}$	$0.0402e^{i242.0}$
(St. Croix)	LCP	$0.0036e^{i11.8}$	$0.0089e^{i24.2}$	$0.0805e^{i318.9}$	$0.0596e^{i183.5}$

[a] D–terms at 5 GHz; [b] D–terms at 8.4 GHz; [c] D–terms at 22 GHz; [d] D–terms at 43 GHz; [e] OV did not observe at 8.4 and 22 GHz

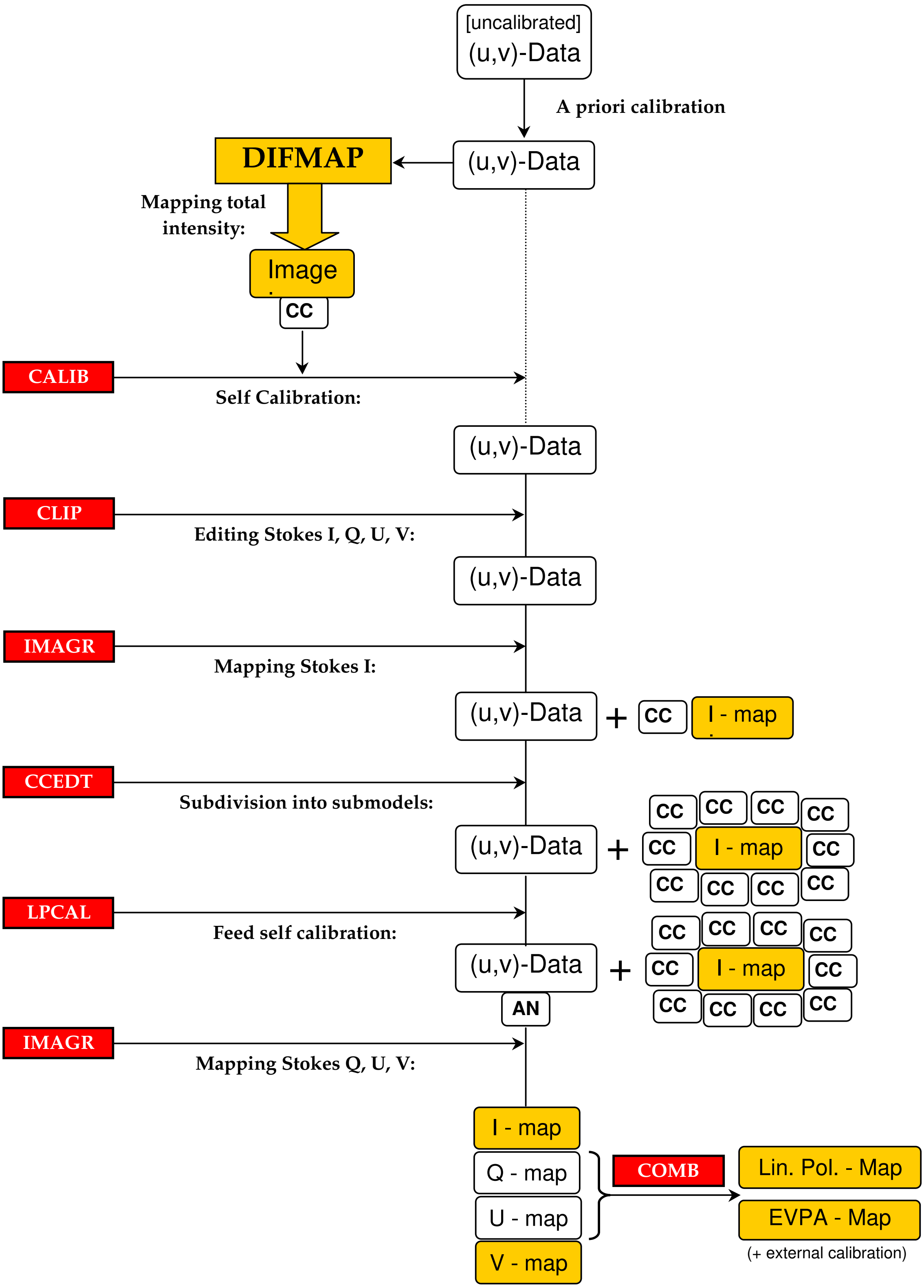

Figure 3.10: The basic feed self–calibration path in $\mathcal{AIPS}$.

Bibliography

Barth, A. J., Filippenko, A. V., & Moran, E. C. 1999, Astrophys. J., 515, L61

Becklin, E. E., Tokunaga, A. T., & Wynn-Williams, C. G. 1982, Astrophys. J., 263, 624

Blandford, R. D. & Königl, A. 1979, Astrophys. J., 232, 34

Blumenthal, G. R. & Gould, R. J. 1970, Reviews of Modern Physics, 42, 237

Braatz, J. A., Wilson, A. S., & Henkel, C. 1996, Astrophys. J. Suppl., 106, 51

Brown, R. L. 1987, in Spectroscopy of Astrophysical Plasmas, 35–58

California Institute of Technology. 1991, BAAS, 23, 991

Claussen, M. J., Diamond, P. J., Braatz, J. A., Wilson, A. S., & Henkel, C. 1998, Astrophys. J., 500, L129

Condon, J. J., Condon, M. A., Gisler, G., & Puschell, J. J. 1982, Astrophys. J., 252, 102

Daly, R. A. & Marscher, A. P. 1988, Astrophys. J., 334, 539

de Vries, W. H., Barthel, P. D., & O'Dea, C. P. 1997, Astron. & Astrophys., 321, 105

Eckart, A. & Genzel, R. 1996, Nature, 383, 415

Falcke, H. & Biermann, P. L. 1995, Astron. & Astrophys., 293, 665

Falcke, H., Wilson, A. S., & Simpson, C. 1998, Astrophys. J., 502, 199

Fomalont, E. 1981, Newsletter. NRAO No. 3, p. 3, 1981, 3, 3

Forbes, D. A., Georgakakis, A. E., & Brodie, J. P. 2001, Monthly Not. Roy. Astron. Soc., 325, 1431

Fosbury, R. A. E., Mebold, U., Goss, W. M., & Dopita, M. A. 1978, Monthly Not. Roy. Astron. Soc., 183, 549

Gómez, J. L., Marscher, A. P., Alberdi, A., Jorstad, S. G., & García-Miró, C. 2000, Science, 289, 2317

Gabel, J. R., Bruhweiler, F. C., Crenshaw, D. M., Kraemer, S. B., & Miskey, C. L. 2000, Astrophys. J., 532, 883

Gallagher, J. S. 1986, Publ. Astron. Soc. Pacific, 98, 81

Georganopoulos, M. & Marscher, A. P. 1996, in ASP Conf. Ser. 100: Energy Transport in Radio Galaxies and Quasars, 67

Guainazzi, M. & Antonelli, L. A. 1999, Monthly Not. Roy. Astron. Soc., 304, L15

Guainazzi, M., Oosterbroek, T., Antonelli, L. A., & Matt, G. 2000, Astron. & Astrophys., 364, L80

Harris, D. E., Carilli, C. L., & Perley, R. A. 1994, Nature, 367, 713

Harris, D. E. & Krawczynski, H. 2002, Astrophys. J., 565, 244

Heeschen, D. S. 1970, Astron. J., 75, 523

Heeschen, D. S. & Puschell, J. J. 1983, Astrophys. J., 267, L11

Ho, L. C., Filippenko, A. V., & Sargent, W. L. 1995, Astrophys. J. Suppl., 98, 477

Ho, L. C., Filippenko, A. V., & Sargent, W. L. W. 1997, Astrophys. J. Suppl., 112, 315

Högbom, J. A. 1983, in Indirect Imaging. Measurement and Processing for Indirect Imaging. Proceedings of an International Symposium held in Sydney, Australia, August 30-September 2, 1983. Editor, J.A. Roberts; Publisher, Cambridge, England, New York, USA, Cambridge University Press, 1984, 247

Johnston, K. J., Fey, A. L., Zacharias, N., Russell, J. L., Ma, C., de Vegt, C., Reynolds, J. E., Jauncey, D. L., Archinal, B. A., Carter, M. S., Corbin, T. E., Eubanks, T. M., Florkowski, D. R., Hall, D. M., McCarthy, D. D., McCulloch, P. M., King, E. A., Nicolson, G., & Shaffer, D. B. 1995, Astron. J., 110, 880

Jones, D. L., Tingay, S. J., Murphy, D. W., Meier, D. L., Jauncey, D. L., Reynolds, J. E., Tzioumis, A. K., Preston, R. A., McCulloch, P. M., Costa, M. E., Kemball, A. J., Nicolson, G. D., Quick, J. F. H., King, E. A., Lovell, J. E. J., Clay, R. W., Ferris, R. H., Gough, R. G., Sinclair, M. W., Ellingsen, S. P., Edwards, P. G., Jones, P. A., van Ommen, T. D., Harbison, P., & Migenes, V. 1996, Astrophys. J., 466, L63

Jones, D. L., Wehrle, A. E., Meier, D. L., & Piner, B. G. 2000, Astrophys. J., 534, 165

Jones, D. L., Wrobel, J. M., & Shaffer, D. B. 1984, Astrophys. J., 276, 480

Kameno, S., Sawada-Satoh, S., Inoue, M., Shen, Z., & Wajima, K. 2001, Publ. Astron. Soc. Japan, 53, 169

Kellermann, K. I., Vermeulen, R. C., Cohen, M. H., & Zensus, J. A. 1999, in American Astronomical Society Meeting, Vol. 194, #20.02

Kellermann, K. I., Vermeulen, R. C., Zensus, J. A., & Cohen, M. H. 1998, Astron. J., 115, 1295

Kemball, A. J., Diamond, P. J., & Cotton, W. D. 1995, Astron. &. Astrophys. Suppl., 110, 383

Knapp, G. R., Faber, S. M., & Gallagher, J. S. 1978, Astron. J., 83, 139

Krichbaum, T. P., Alef, W., Witzel, A., Zensus, J. A., Booth, R. S., Greve, A., & Rogers, A. E. E. 1998, Astron. & Astrophys., 329, 873

Krolik, J. H. 1999, Active galactic nuclei : from the central black hole to the galactic environment (Princeton, NJ, USA : Princeton University Press, 1999.)

Leppänen, K. J., Zensus, J. A., & Diamond, P. J. 1995, Astron. J., 110, 2479

Levinson, A., Laor, A., & Vermeulen, R. C. 1995, Astrophys. J., 448, 589+

Lobanov, A. P. 1998, Astron. & Astrophys., 330, 79

Marr, J. M., Taylor, G. B., & Crawford, F. 2000, in Astrophysical Phenomena Revealed by Space VLBI, Proceedings of the VSOP Symposium, held at the Institute of Space and astronautical Science, Sagamihara, Kanagawa, Japan, January 19 - 21, 2000, Eds.: H. Hirabayashi, P.G. Edwards, and D.W. Murphy, Sagamihara, Kanagawa, Japan: Institute of Space and astronautical Science, 2000, 91

Mayall, N. U. 1939, Lick Observatory Bulletin, 497, 33

McDowell, J. C. 1994, in Einstein Obs. Unscreened IPC Data Archive

Mirabel, I. F. & Rodríguez, L. F. 1999, Annu. Rev. Astron. Astrophys., 37, 409

Miyoshi, M., Moran, J., Herrnstein, J., Greenhill, L., Nakai, N., Diamond, P., & Inoue, M. 1995, Nature, 373, 127

Napier, P. J. 1994, in IAU Symp. 158: Very High Angular Resolution Imaging, Vol. 158, 117

Omar, A., Anantharamaiah, K. R., Rupen, M., & Rigby, J. 2002, Astron. & Astrophys., 381, L29

Pearson, T. J., Shepherd, M. C., Taylor, G. B., & Myers, S. T. 1994, in American Astronomical Society Meeting, Vol. 185, #08.08

Peterson, B. M. 1997, An introduction to active galactic nuclei (Cambridge, UK, New York, USA: Cambridge University Press)

Pogge, R. W., Maoz, D., Ho, L. C., & Eracleous, M. 2000, Astrophys. J., 532, 323

Ros, E. 1997, Astrometría diferencial de precisión con VLBI en el triángulo de Draco (y estudios de SN 1993J) (València, Spain: Servicio de Publicaciones, Universitat de València), 35

Rybicki, G. B. & Lightman, A. P. 1979, Radiative Processes in Astrophysics (New York, USA: Wiley-Interscience)

Schwartz, D. A., Marshall, H. L., Lovell, J. E. J., Piner, B. G., Tingay, S. J., Birkinshaw, M., Chartas, G., Elvis, M., Feigelson, E. D., Ghosh, K. K., Harris, D. E., Hirabayashi, H., Hooper, E. J., Jauncey, D. L., Lanzetta, K. M., Mathur, S., Preston, R. A., Tucker, W. H., Virani, S., Wilkes, B., & Worrall, D. M. 2000, Astrophys. J., 540, L69

Smith, D. A., Wilson, A. S., Arnaud, K. A., Terashima, Y., & Young, A. J. 2002, Astrophys. J., 565, 195

Thompson, A. R., Moran, J. M., & Swenson, G. W. 1986, Interferometry and synthesis in radio astronomy (New York, Wiley-Interscience)

Tingay, S. J. & Murphy, D. W. 2001, Astrophys. J., 546, 210

Van Gorkom, J. H., Knapp, G. R., Raimond, E., Faber, S. M., & Gallagher, J. S. 1986, Astron. J., 91, 791

Vermeulen, R. C., Readhead, A. C. S., & Backer, D. C. 1994, Astrophys. J., 430, L41

Vermeulen, R. C., Ros, E., Kellermann, K. I., Cohen, M. H., & Zensus, J. A. 2002, in prep.

Wagner, S. J. & Witzel, A. 1995, Annu. Rev. Astron. Astrophys., 33, 163

Weaver, K. A., Wilson, A. S., Henkel, C., & Braatz, J. A. 1999, Astrophys. J., 520, 130

Wells, D. C., Greisen, E. W., & Harten, R. H. 1981, Astron. &. Astrophys. Suppl., 44, 363

Wilson, A. S. & Yang, Y. 2002, Astrophys. J., 568, 133

Wilson, A. S., Young, A. J., & Shopbell, P. L. 2000, Astrophys. J., 544, L27

Wrobel, J. M. 1984, Astrophys. J., 284, 531

Young, A. J., Wilson, A. S., Terashima, Y., Arnaud, K. A., & Smith, D. A. 2002, Astrophys. J., 564, 176

Yusef-Zadeh, F., Melia, F., & Wardle, M. 2000, Science, 287, 85

Zensus, J. A. 1997, Annu. Rev. Astron. Astrophys., 35, 607

Zensus, J. A., Ros, E., Kellermann, K. I., Cohen, M. H., Vermeulen, R. C., & Kadler, M. 2002, in press (Astron. J., issue August 2002)